Multiple diffraction data analysis for macromolecular crystals in stereoscopic multibeam imaging

Chun-Hsiung Chao,[a,b] Chi-Yuan Hung,[a] Yi-Shan Huang,[a] Chia-Hung Ching,[a] Yen-Ru Lee,[a] Yuch-Chen Jean,[b] Shu-Ching Lai,[a] Yuri P. Stetsko,[a,c] Hanna Yuan[d] and Shih-Lin Chang[a,b]*

[a]Department of Physics, National Tsing Hua University, Hsinchu, Taiwan 300, [b]Synchrotron Radiation Research Center, Hsinchu, Taiwan 300, [c]Chernovtsy State University, Chernovtsy 274012, Ukraine, and [d]Institute of Molecular Biology, Academia Sinica, Taipei, Taiwan 100. Correspondence e-mail: slchang@phys.nthu.edu.tw

A detailed analysis of multiple diffraction data collected by the stereoscopic multibeam imaging technique from a tetragonal lysozyme crystal is reported. Calculations based on the dynamical theory are employed to account for diffraction profiles obtained with Bragg-angle scan in stereoscopic imaging and the conventional azimuthal scan in Renninger arrangement. The formation of a multibeam intensity profile and the relationship and mutual influence between the two scans are investigated. A simple practical method of quantitative estimation of the reflection phases of structure-factor multiplets from the experimental data obtained with two inversion-symmetry-related diffractions is proposed. The procedures for data handling and for distinguishing 'partial' diffraction images from 'full' diffraction images are also developed considering multibeam diffraction geometry and experimental conditions. These procedures thus provide a practical way of reconstructing diffraction profiles for experimental phase determination for macromolecular crystals.

1. Introduction

Recent progress in the development of the multiple diffraction technique has demonstrated the possibility of directly determining the phases of structure-factor multiplets, mainly triplets, from intensity measurements (see, for example, Chang, 1987, and references therein; Colella, 1992, and references therein; Weckert & Hümmer, 1997, and references therein; Chang, 1998, and references therein; Mo *et al.*, 1998). For applications to crystal-structure analysis, collecting a large number of multibeam diffractions is needed. This can be achieved in an accumulative manner by using the Renninger scan (Han & Chang, 1983; Chang *et al.*, 1991; Weckert *et al.*, 1999; Chang, Stetsko *et al.*, 1999; Wang *et al.*, 2001) or in a short period by using the reference beam (Shen, 1998; Shen *et al.*, 2000) and the stereoscopic multibeam imaging/detection (Chang *et al.*, 1998; Chang, Chao *et al.*, 1999). The combination of multiple diffraction techniques with other methods, such as direct methods (Schenk, 1991), maximum-entropy methods (Bricogne & Gilmore, 1990) and similar approaches, has led to phase extension and the determination of electron-density maps (Han & Chang, 1983; Chang & Wang, 1996; Hölzer *et al.*, 2000; Weeks *et al.*, 2000; Wang *et al.*, 2001). However, there is still a necessity to improve this diffraction technique to handle a large number of multibeam diffractions and find useful reflections and structure-factor multiplets for phase estimation. In this paper, we report a simple practical method for quantitative estimation of the reflection phases and also a data-analysis procedure developed for stereoscopic imaging so as to reconstruct phase-sensitive diffraction intensity distributions and profiles. This procedure includes data handling, background subtraction and intensity normalization. The method of distinguishing the 'full' multiple diffraction from the 'partial' one is also considered with the aid of dynamical calculation. In addition, an analytical way of finding the angular positions for the stereoscopic pair of the multiple diffraction is also derived from the orientation matrices of the crystal relative to the diffractometer used.

2. Experimental aspects of stereoscopic multibeam imaging

Multiple diffraction occurs when two or more sets of atomic planes are brought simultaneously into position to diffract an incident beam. In reciprocal space, more than two reciprocal-lattice points are rotated onto the surface of an Ewald sphere at the same time. Usually, the rotation involves the Bragg angle, θ (or ω), of a given reflection and the azimuth angle, ψ, around the reciprocal-lattice vector of the same reflection. In analogy with optical holography, each diffracted beam of multiple diffraction can be treated as a reference beam for the others and the interference among the diffracted beams gives rise to intensity variation of each diffracted beam, which

provides phase information. Various diffraction geometries, accompanied by different detector systems, for generating multiple diffraction have been developed, including the Renninger (azimuthal) scan (Renninger, 1937), the Kossel diagram (Kossel, 1936), the reference beam (Kov'ev *et al.*, 1984; Shen, 1998), stereoscopic imaging/detection (Chang *et al.*, 1998; Chang, Chao *et al.*, 1999) and others. For the stereoscopic multibeam imaging/detection, two inversion-symmetry-related (ISR) reflections are used to generate multiple diffraction, *i.e.* the Friedel pairs of multiple diffraction, for quasi-two-dimensional (2D) (Chang *et al.*, 1998) and three-dimensional (3D) crystals (Chang, Chao *et al.*, 1999). Fig. 1 shows the schematic representation of this technique for the two ISR three-beam diffractions, (O, G, L) and $(O, -G, -L)$, in 3D lattices. For each of the three-beam cases, say (O, G, L), the intensity of the secondary L reflection (or the primary G reflection) is considered as a reference background for revealing the interference between the primary G and the secondary L reflection. Therefore, the crystal needs to be brought first to the vicinity of the Bragg angle, θ_G, of the G reflection. The crystal is then rotated around an axis perpendicular to the plane of incidence of the G reflection by the Bragg angle (ω) scan, denoted as a polar scan, across the exact Bragg diffraction position for the primary G reflection. For each ω angle in the polar ω scan, the crystal needs to be rotated around the reciprocal-lattice vector $\mathbf{g}$ of the G reflection, the azimuthal ψ scan, to bring the reciprocal point of the L reflection to cross the surface of the Ewald sphere, thus generating multiple diffraction. The recorded intensity variation on the reference background of the L reflection *versus* ω (or the angular deviation $\Delta\theta$ from the Bragg angle θ_G of the G reflection) is a multiple-diffraction profile. For the ISR $(O, -G, -L)$ case, the crystal is rotated to a geometrically and crystallographically equivalent position, as mentioned in Chang, Chao *et al.* (1999). The pathway of the reciprocal-lattice point $-L$ crossing the surface of the Ewald sphere is

kept the same as for the reciprocal-lattice point L in the (O, G, L) case. For the eight-circle Huber diffractometer used, the $\varphi - \chi - \psi - \omega$ goniostat, in the order of the stacking of the crystal rotating circles, is adopted. An imaging plate is placed on the detector arm, which can be rotated along the 2θ and γ circles in the vertical and the horizontal plane, respectively. The conventional φ and χ circles are used to align the reciprocal-lattice vector $\mathbf{g}$ along the ψ axis. The origin, $\chi = 0$, of the χ circle is defined as the φ axis lies in the horizontal plane along the $-x$ direction (see Appendix A). The ω circle is used to vary the Bragg angle of the G reflection. The ψ and ω axes lie in the horizontal and the vertical planes, respectively. Suppose that the (O, G, L) diffraction occurs at the angular position ($2\theta = 2\theta_G$, $\theta = \theta_G$, $\varphi = \varphi_O$, $\chi = \chi_O$). There are two ways to bring the $(O, -G, -L)$ case into the right position $(2\theta, \theta, \varphi, \chi)$, which can be calculated from the orientation matrices of the crystal with respect to the diffractometer (see Appendix A):

(i) Keeping the position of the 2D detector unchanged ($2\theta = 2\theta_G$). The crystal needs to be rotated to $\varphi = \pi + \varphi_O$ and $\chi = \pi - \chi_O$. Therefore, the position for the $(O, -G, -L)$ case is ($2\theta = 2\theta_G$, $\theta = \theta_G$, $\varphi = \pi + \varphi_O$, $\chi = \pi - \chi_O$). During the X-ray exposure, the direction of the ψ rotation around $-\mathbf{g}$ should be opposite to that for $\mathbf{g}$ in the (O, G, L) case. This means that for the images of the secondary reflections L in the (O, G, L) case originally appearing in the upper half of the 2D detector above the $\mathbf{g}$ vector, their counterparts $-L$ in the $(O, -G, -L)$ case appear in the lower part and *vice versa*. Under this situation, the pathways of the secondary reciprocal lattices in both cases are the same, except that one enters (or leaves) the Ewald sphere from the upper hemisphere and the other leaves (or enters) from the lower hemisphere.

(ii) Changing the detector position from 2θ to -2θ. The crystal needs to be rotated to $\varphi = \pi + \varphi_O$, and $\chi = -\chi_O$. Therefore, the position for the $(O, -G, -L)$ case is ($2\theta = -2\theta_G$, $\theta = -\theta_G$, $\varphi = \pi + \varphi_O$, $\chi = -\chi_O$). The direction of the ψ rotation around $-\mathbf{g}$ is the same as that for $\mathbf{g}$ in the (O, G, L) case. This means that, for the images of the secondary reflections L in the (O, G, L) case appearing on the left hemisphere, their counterparts $-L$ in the $(O, -G, -L)$ case appear on the right hemisphere.

Similar positions can be found for a conventional four-circle diffractometer by using an appropriate orientation matrix.

Multiple diffraction results from the interaction of the primary G, the secondary L and the coupling $G-L$ reflection. The intensity variations, recorded as the diffraction profiles, of the two ISR three-beam cases are thus related to the triplet phases $\delta_{3(L)}$ or $\delta_{3(G)}$, depending on whether L or G is the reference. The phases $\delta_{3(L)} = \delta_G + \delta_{L-G} - \delta_L$ and $\delta_{3(G)} = \delta_L + \delta_{G-L} - \delta_G$, where δ_H is the phase of the individual H reflection ($H = G, L, G - L, L - G$). For negligibly small dispersion corrections, $\delta_{3(L)} = \delta_{3(-G)} = -\delta_{3(-L)} = -\delta_{3(G)}$. For a systematic four-beam (O, G, L_1, L_2) case, involving a 2 or 2_1 axis, the dominant triplet phase is still the δ_3 (Hümmer *et al.*, 1991).

Fig. 2 shows typical four-beam multiple-diffraction patterns $I_{L_1}(\Delta\theta)$ and $I_{-L_1}(\Delta\theta)$, the $\Delta\theta$ distribution of the four-beam
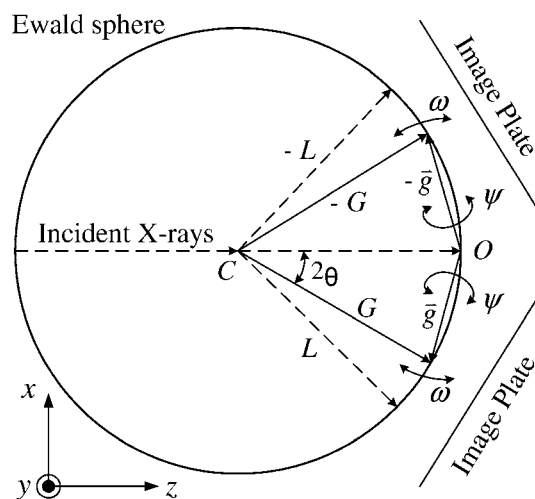

Figure 1
Schematic representation of the stereoscopic multibeam imaging technique.

intensities normalized by the corresponding two-beam intensities, for two ISR cases (000; 200; 12, 2, $\bar{1}$; $\overline{10}$, 2, $\bar{1}$ and (000; $\bar{2}$00; $\overline{12}$, $\bar{2}$, 1; 10, $\bar{2}$, 1) of tetragonal hen-egg white lysozyme (file 1Lyz in the Protein Data Bank) obtained with the stereoscopic imaging technique. The crystal oscillation range around $\mathbf{g}$ = [200] and $-\mathbf{g}$ = [$\bar{2}$00] is $\Delta\psi$ = 2° and $I_{L_1}(\Delta\theta)$ [$= \int I_{L_1}(\Delta\theta, \Delta\psi)\,\mathrm{d}(\Delta\psi)$] and $I_{-L_1}(\Delta\theta)$ are the four-beam integrated intensities over $\Delta\psi$. Synchrotron radiation at λ = 1.24 Å is used and the distance between the crystal and the imaging plate is about 10 cm. The crystal size is around 0.2 mm in diameter.

3. Dynamical calculations

The dynamical calculation algorithm using the Cartesian coordinate system (Stetsko & Chang, 1997) for X-ray wavefields is adopted to investigate the behavior of multiple diffraction in macromolecular crystals and to account for the intensity distributions measured. The influence of overlapping of neighboring multiple diffractions on multiply diffracted intensities is studied. The diffraction intensities for different diffraction geometry are calculated. The results are described below.
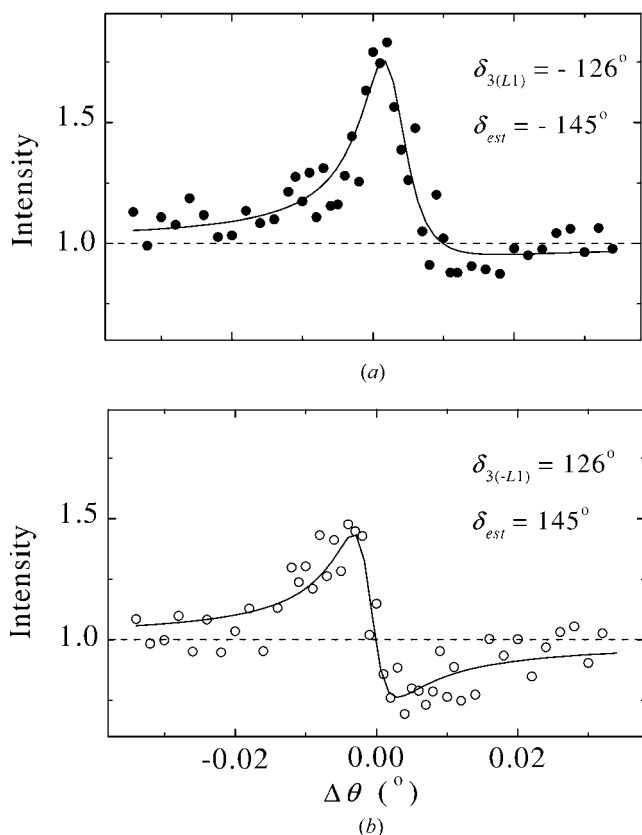

Figure 2
$\Delta\theta$ distribution of measured semi-integrated relative intensities for (a) $L_1(12, 2, \bar{1})$ and (b) $-L_1(\overline{12}, \bar{2}, 1)$ reflections of two ISR cases (000; 200; 12, 2, $\bar{1}$; $\overline{10}$, 2, $\bar{1}$) and (000; $\bar{2}$00; $\overline{12}$, $\bar{2}$, 1; 10, $\bar{2}$, 1), respectively.

3.1. Mutual influence of neighboring multiple diffraction

Owing to the comparably large lattice parameters for macromolecular crystals, a large number of multiple diffractions take place very often in a very small angular range of crystal rotation. Overlapping among many multiple diffractions is unavoidable. It is known that multiple diffraction is systematic if the same multibeam case occurs for all X-ray wavelengths, as long as the involved reciprocal-lattice points, lying in one plane, can be brought simultaneously onto the surface of the corresponding Ewald sphere (Chang, 1984). In contrast to systematic multiple diffraction, a multibeam case with involved reciprocal-lattice points not lying in one plane, which can take place only at a specific wavelength, is called coincidental multiple diffraction. In a Renninger scan, the overlap of two systematic multiple diffractions gives rise to a coincidental multibeam situation. For example, if two systematic three-beam cases overlap with each other at a given wavelength, then a four-beam coincidental diffraction is formed at that wavelength. The corresponding multibeam interaction of the latter is different from that of systematic cases. The intensity distribution and the dominant multiplet phases are therefore different. This influence between two or more overlapped multibeam cases could lead to misinterpretation of phases when analyzing the intensity distribution and the diffraction profile. To eliminate the overlapping, one can increase the wavelength of the incident radiation from hard to soft X-rays so as to decrease the number of multiple diffractions generated. However, the diffraction suffers from strong absorption in the air for soft X-rays and the crystal is more radiation damaged than for hard X-rays. Or one can choose a multiple diffraction with the product of the structure-factor moduli of the secondary and coupling reflections comparable with that of the primary reflection so that the influence of the overlapped cases involving weak reflections is negligibly small (see Weckert & Hümmer, 1997, and references therein). Unfortunately, under this condition, a large number of primary reflections are needed to generate a large number of multiple diffractions. This is of course experimentally not very convenient.

Here we propose a technique to eliminate overlapping by collecting multiple diffractions involving a comparably strong primary reflection and weaker secondary and coupling reflections using the stereoscopic multibeam imaging technique. The integrated intensities over azimuthal angle are measured. As described below, this kind of intensity integration suppresses the influence of neighboring multiple diffraction on the intensity of the measured secondary reflection. In this way, collecting a large set of multibeam diffraction data using only one primary reflection can be achieved. The following is the reasoning that supports this idea.

The mutual influence of neighboring multiple diffraction for different kinds of crystal rotation and integration is numerically verified for the coincidental four-beam ($O(000)$; $G(004)$; $L_1(1, 12, 2)$; $L_2(1, \overline{12}, 2)$) diffraction that consists of two systematic three-beam ($O(000)$; $G(004)$; $L_1(1, 12, 2)$) and ($O(000)$; $G(004)$; $L_2(1, \overline{12}, 2)$) diffractions. This four-beam

coincidental diffraction occurs at the wavelength $\lambda = 1.2374$ Å. The primary reflection G is stronger than the secondary (L_1 and L_2) and coupling ($G - L_1$, $G - L_2$ and $L_1 - L_2$) reflections because the structure-factor moduli are $|F_{004}| = 1372$, $|F_{1,12,2}| = 473$ and $|F_{0,24,0}| = 428$ electrons. Fig. 3 shows the calculated two-dimensional ($\Delta\theta, \Delta\psi$) intensity distributions for (a) $I_G(\Delta\theta, \Delta\psi)$ of the symmetrical Laue primary G reflection and (b) $I_{L_1}(\Delta\theta, \Delta\psi)$ and (c) $I_{L_2}(\Delta\theta, \Delta\psi)$
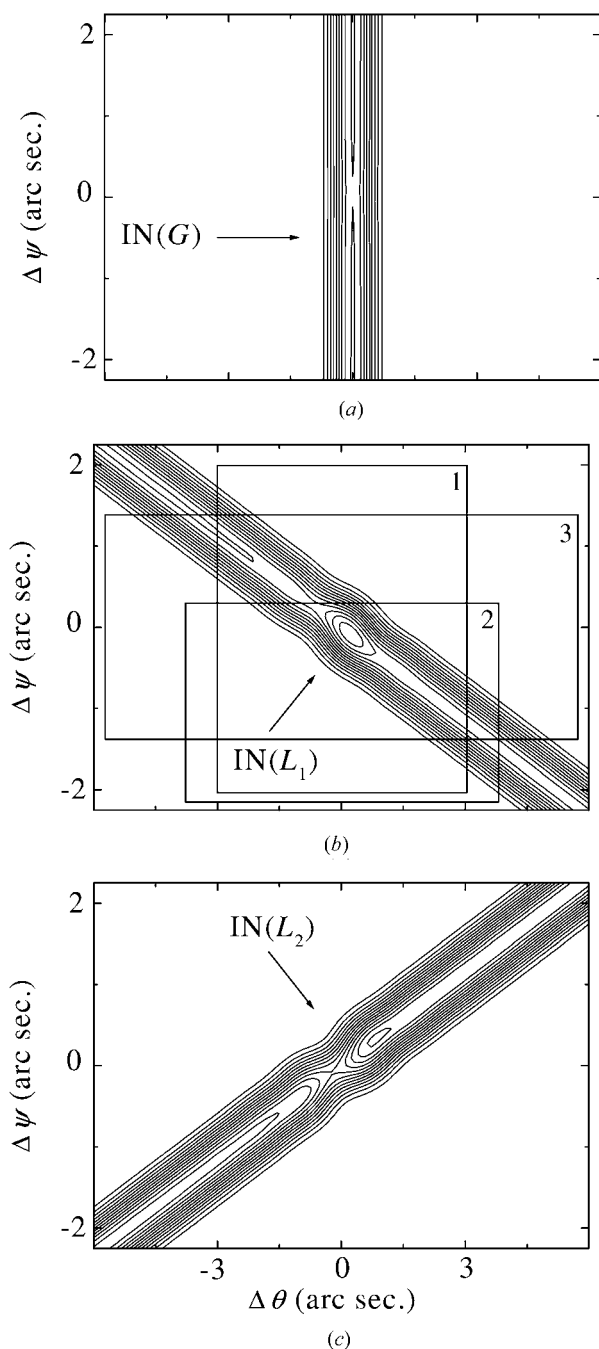
of non-symmetrical Laue secondary L_1 and L_2 reflections around the four-beam diffraction position. The crystal plate is 0.2 mm thick. The arrows IN(G), IN(L_1) and IN(L_2) show the directions of the crystal rotation that correspond to the movement of the reciprocal-lattice points G, L_1 and L_2 towards the interior of the Ewald sphere. Fig. 4 shows the calculated relative intensity profiles for (a) $I_G(\Delta\theta)$, (b) $I_{L_1}(\Delta\theta)$
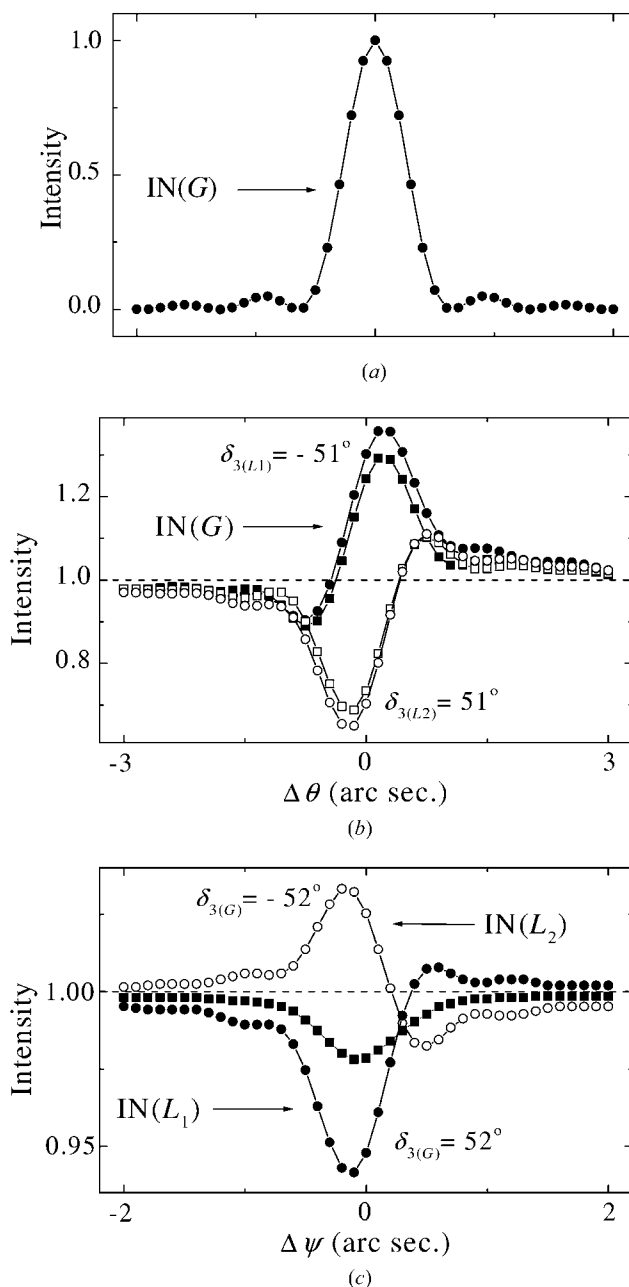

Figure 3
Calculated two-dimensional ($\Delta\theta, \Delta\psi$) intensity distribution for the four-beam (000; 004; 1, 12, 2; 1, $\overline{12}$, 2) coincidental Laue–Laue diffraction. (a) G(004) primary reflection, (b) L_1(1, 12, 2) and (c) L_2(1, $\overline{12}$, 2) secondary reflections.

Figure 4
Calculated semi-integrated relative intensity profiles for the case of Fig. 3. (a) $\Delta\theta$ distribution of the G(004) reflection, (b) $\Delta\theta$ distribution of the L_1(1, 12, 2) reflection [solid squares: four-beam case; solid circles: three-beam (000; 004; 1, 12, 2) case] and the L_2(1, $\overline{12}$, 2) reflection [open squares: four-beam case; open circles: three-beam (000; 004; 1, $\overline{12}$, 2) case], and (c) $\Delta\psi$ distribution of the G(004) reflection [solid squares: four-beam case; solid and open circles: three-beam (000; 004; 1, 12, 2) and (000; 004; 1, $\overline{12}$, 2) cases, respectively].

and $I_{L_2}(\Delta\theta)$ integrated over $\Delta\psi$, and for (c) $I_G(\Delta\psi) = \int I_G(\Delta\theta, \Delta\psi)\,d(\Delta\theta)$ integrated over $\Delta\theta$. In Fig. 4(b), the curves with solid and open squares are the intensity profiles of $L_1(1, 12, 2)$ and $L_2(1, \overline{12}, 2)$ in the four-beam case, respectively. The curves with solid and open circles are the profiles of $L_1(1, 12, 2)$ and $L_2(1, \overline{12}, 2)$ in the corresponding three-beam cases, respectively. In Fig. 4(c), the curve with solid squares is the profile of the $G(004)$ in the four-beam case. The curves with solid and open circles are the profiles of the $G(004)$ for the three-beam cases involving $L_1(1, 12, 2)$ and $L_2(1, \overline{12}, 2)$,

Figure 5
$\Delta\theta$ distribution of calculated semi-integrated relative intensities for the $L_1(12, 2, \overline{1})$ (solid circles) and the $-L_1(\overline{12}, \overline{2}, 1)$ (open circles) reflections of the two ISR cases of Fig. 2. $|F_{200}| = 2846$, $|F_{12,2,1}| = 457$, $|F_{10,2,1}| = 1200$ and $|F_{22,0,0}| = 390$.

respectively. The difference between the $\Delta\theta$ distributed profiles $I_{L_1}(\Delta\theta)$ [the same for $I_{L_2}(\Delta\theta)$] calculated for the four-beam case (squares in Fig. 4b) and for the three-beam cases (circles in Fig. 4b) is small, while the same difference for the $\Delta\psi$ distributed profiles $I_G(\Delta\psi)$ (squares and circles in Fig. 4c) is appreciably larger. Thus, for a comparably strong primary reflection, in contrast to the Renninger (azimuthal) $\Delta\psi$ scan, the polar $\Delta\theta$ scan in the stereoscopic multibeam imaging technique with the integration over angle $\Delta\psi$ suppresses the influence of neighboring multiple diffractions on the intensity of the secondary reflection.

The dynamical calculation also shows that for a comparably strong primary reflection the same behavior mentioned also takes place for a systematic four-beam (O, G, L_1, L_2) diffraction. That is, the presence of the reflection L_2 practically does not affect the intensity $I_{L_1}(\Delta\theta)$ of the reflection L_1 [just as L_1 does not affect $I_{L_2}(\Delta\theta)$] obtained in the stereoscopic multibeam imaging technique. Therefore, in this imaging technique, the triplet phase $\delta_{3(L1)}$ plays a dominant role in affecting the intensity $I_{L_1}(\Delta\theta)$, independent of the space-group symmetry. So does the $\delta_{3(L2)}$ in $I_{L_2}(\Delta\theta)$. Thus, direct phase estimation of the triplet phase $\delta_{3(L1)}$ or $\delta_{3(L2)}$ from the four-beam diffraction profiles is feasible without the involvement of a 2 or 2_1 axis in the crystal rotation mentioned in §2.
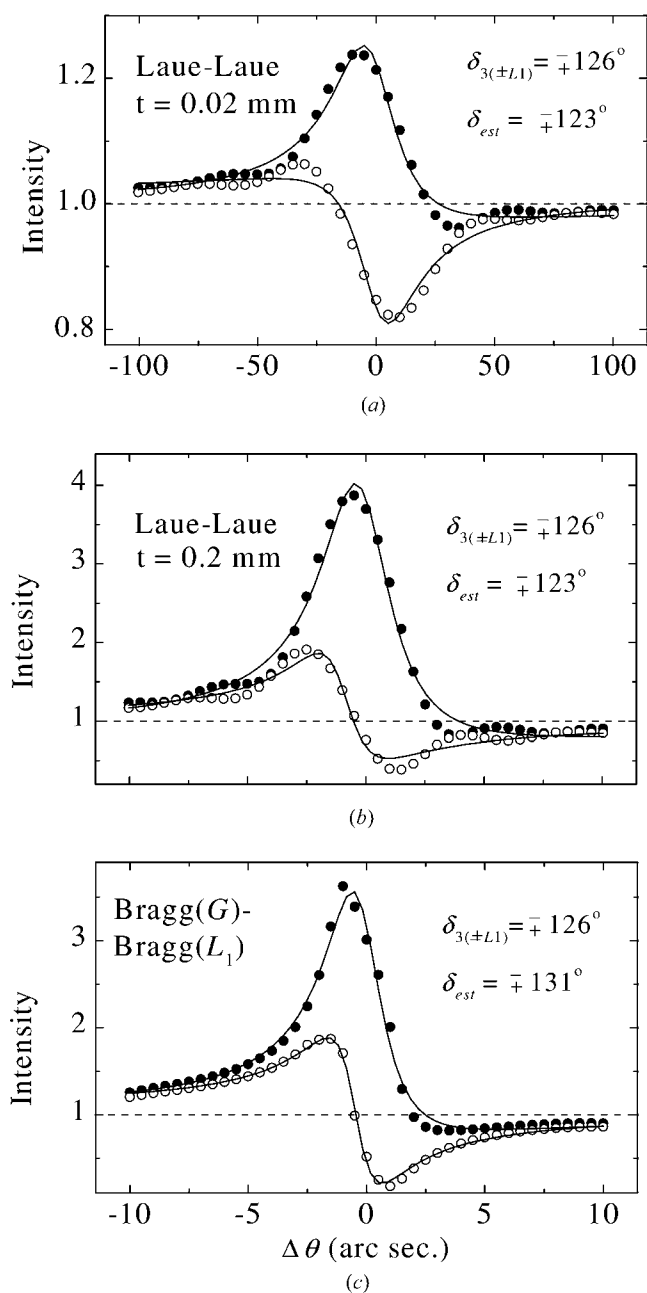
3.2. Influence of diffraction geometry

The Laue–Laue and Bragg–Bragg diffraction geometry are studied for crystal plates with finite and semi-infinite thickness, where the primary and secondary reflections are all Laue and all Bragg cases, respectively. In practice, since the sizes of macromolecular crystals are usually smaller than the X-ray beam size, multiple diffraction could be a mixing of Laue and Bragg diffraction. Therefore, the proposed calculation approach is an approximation to the real situation. The dynamical calculation for different diffraction geometry is made for the two ISR systematical four-beam diffraction cases $(O(000);\ G(200);\ L_1(12, 2, \overline{1});\ L_2(\overline{10}, 2, \overline{1}))$ and $(O(000);\ -G(\overline{2}00);\ -L_1(\overline{12}, \overline{2}, 1);\ -L_2(10, \overline{2}, 1))$. The experimental profiles are shown in Fig. 2 for comparison.

Fig. 5 shows the semi-integrated profiles over $\Delta\theta$ for these two ISR cases, calculated for 0.02 and 0.2 mm thick crystals in a Laue–Laue geometry (Figs. 5a and 5b) and for a semi-infinite crystal in a Bragg(G)–Bragg(L_1) geometry, respectively. For the former, the primary reflections $\pm G$ are symmetrical Laue and $\pm L_1$ and $\pm L_2$ are inclined Laue (Figs. 5a and 5b). For the latter, $\pm G$ are symmetrical Bragg, $\pm L_1$ inclined Bragg, and $\pm L_2$ inclined Laue cases (Fig. 5c). As can be seen in Fig. 5, the multiple-diffraction profiles show qualitatively similar behaviors in different diffraction geometries (see also Weckert & Hümmer, 1997, and references therein). Owing to the mixing of these geometries for the diffraction from a small macromolecular crystal, this outcome is very important for reliable interpretation of the obtained experimental profiles. In particular, our calculated results are in good qualitative agreement with the experimental ones shown in Fig. 2, except for the profile widths. It should also be noted (see Thorkildsen

research papers

et al., 2001, and references therein) that for reliable phase estimation from Laue–Laue diffraction, which seems to play a dominant role in diffraction from macromolecular crystals, a crystal thickness smaller than the extinction length should be used. This length is usually of the order of millimetres for traditional X-ray wavelengths used.

The widths of multiple-beam profiles calculated for the Laue–Laue diffraction of a 0.02 mm thick crystal plate (Fig. 5a) are similar to those of the experimental profiles (Fig. 2) for a 0.2 mm thick crystal. However, the widths of the Laue–Laue diffraction for a 0.2 mm thick crystal (Fig. 5b) and of the Bragg–Bragg diffraction for a semi-infinitely thick crystal (Fig. 5c) are smaller. The broadening of the experimental profiles is, as usual, due to crystal mosaicity and spectral and angular divergences of the incident beam.

Although the results obtained from this approach agree well with the experimental ones, for a more precise description of diffraction intensity from macromolecular crystals, the multibeam dynamical calculation for crystals of a finite shape may be used (see, for example, Thorkildsen & Larsen, 1998; Larsen & Thorkildsen, 1998a,b; Thorkildsen et al., 2001).

4. Quantitative estimation of triplet reflection phases

According to Chang, Chao et al. (1999), the relative intensity $I_L(\Delta\theta)$ integrated over $\Delta\psi$ in stereoscopic imaging can be approximately expressed in terms of the phase-dependent $I_D(\Delta\theta)$ and the phase-independent $I_K(\Delta\theta)$ distributions as

$$I_L(\Delta\theta) = I_D(\Delta\theta) + I_K(\Delta\theta), \quad (1)$$

where

$$I_D(\Delta\theta) = q[\Delta\theta \cos\delta_{3(L)} - p\sin\delta_{3(L)}]/[(\Delta\theta)^2 + p^2] \quad (2)$$

and

$$I_K(\Delta\theta) = rp/[(\Delta\theta)^2 + p^2], \quad (3)$$

which is a Lorentzian. p is the FWHM of the Lorentzian. q and r are the factors related to the Lorentz–polarization factor and the structure-factor triplet $|F_G||F_{L-G}|/|F_L|$ (Chang & Tang, 1988). It has been shown that, based on the analysis of the intensity extrema of multiple diffraction profiles for the ISR Friedel pairs in the Renninger geometry (the azimuthal scan around the vector **g** of the primary reflection G), a simple intensity-ratio formula was proposed by Chang, Stetsko et al. (1999) for direct quantitative estimation of reflection phase. Namely,

$$\tan\delta_{3(G)} = [K_-^{1/2} - K_-^{-1/2} - (K_+^{1/2} - K_+^{-1/2})]/4, \quad (4)$$

where $K_\pm = |I_{max}^\pm/I_{min}^\pm|$ are the intensity ratios of the maximum and minimum of the profiles for the +, i.e. (O, G, L), and −, $(O, -G, -L)$, three-beam cases. Owing to relatively large fluctuations in the intensity measurement of comparably weak secondary reflections in stereoscopic multibeam imaging, the use of intensity extrema for reliable phase analysis is difficult. Therefore, in the present paper, the intensity-ratio approach for quantitative phasing in polar scan is modified. The modification consists in the best fit of the

experimental (or calculated) profiles, $I_L(\Delta\theta)$, for the two ISR cases to 'asymmetrical' Lorentzian functions defined as

$$L_\pm(\Delta\theta) = [a_\pm(\Delta\theta - \Delta\theta_\pm) - b_\pm]/[(\Delta\theta - \Delta\theta_\pm)^2 + c_\pm^2], \quad (5)$$

where signs + and − correspond to L and $-L$ cases, respectively. The adjustable parameters are $a_\pm$, $b_\pm$, $c_\pm$ and $\Delta\theta_\pm$, where $\Delta\theta_\pm$ are the zero-point shifts of the Lorentzians. From the relation $\delta_{3(-L)} = -\delta_{3(L)}$ for an ISR Friedel pair and (1)–(3), it follows that $a_+ = a_- \ (\equiv a)$ and $c_+ = c_- \ (\equiv c)$. The parameters a, $b_\pm$ and c from the best fit to (1)–(3) give the following simple form:

$$\tan\delta_{3(L)} = (b_- - b_+)/2ac \quad (6)$$

for the quantitative estimation of the phase $\delta_{3(L)}$ in the stereoscopic multibeam imaging. Results of the best fit to the calculated profiles with Lorentzian functions (5) are shown in Fig. 5 as the solid curves. The estimated values δ_{est} obtained from (6) are in a good agreement (within several degrees) with the values $\delta_{3(\pm L1)}$ calculated from the known structure. Both $\delta_{3(\pm L1)}$ and δ_{est} are indicated in Fig. 5. The same fitting curves (solid) and the values $\delta_{3(\pm L1)}$ and δ_{est} are also given in Fig. 2 for the measured profiles. Investigations on a large number of measured profiles showed that the estimated phase values δ_{est} are on the average within the accuracy of $30°$ compared to the calculated ones. It should be noted that, in practice, owing to errors in the experiments and the theoretical approach in analyzing the diffraction profiles for Friedel pairs, the fitting parameters a_+ and c_+ could differ from a_- and c_-, respectively. In this case, the parameters a and c of (5) can be considered as a weight average for a_+ and a_- and for c_+ and c_-, respectively. In turn, the values $r_a = 1 - |a_+ - a_-|/a$ and $r_c = 1 - |c_+ - c_-|/c$ can serve as the indices of reliability for fitting. For reliable phase determination, the values of r_a and r_c should be close to unity. For the calculated curves shown in Fig. 5, the reliability indices range from 0.83 to 0.98, and for the experimental curves of Fig. 2 the indices are $r_a = 0.8$ and $r_c = 0.75$.

5. 'Full' and 'partial' diffractions

Owing to the experimental conditions for the azimuthal ψ and polar ω scan employed in the stereoscopic imaging, the reciprocal-lattice point of the L reflection could be fully passing through or partially touching the surface of the Ewald sphere. The diffraction images and hence the multiple diffraction profiles are different for 'full' and 'partial' multibeam situations. Only those profiles of 'full' diffraction are useful for phase determination. It is, therefore, important to distinguish when possible the intensity distribution of a 'full' diffraction from a 'partial' one. With the aid of dynamical calculation for $I_L(\Delta\theta, \Delta\psi)$, the discrimination of the 'full' from the 'partial' situation can be achieved with ease and an analytical procedure can be developed for this purpose.

Fig. 3(b) shows different 'full' and 'partial' diffraction situations in rectangles in the $(\Delta\theta, \Delta\psi)$ coordinate system. To facilitate the discussion, the angular ranges covered by the intensity distribution of the diffracted image in $\Delta\theta$ and $\Delta\psi$

confined in a given rectangle are denoted as R_θ and R_ψ. Rectangles 1, 2 and 3 in Fig. 3(b) show the scan ranges for different situations. For rectangle 1, the diffraction intensity line, the inclined line, of the secondary reflection intersects both vertical sides of the rectangle. The case is a 'full' diffraction because the intensity of L_1 is recorded for all the $\Delta\theta$ in R_θ. Namely, the measured range in $\Delta\theta$ is equal to R_θ. For rectangle 2, only the right vertical side intercepts the diffraction line. This case is a 'semi-partial' diffraction because the intensities of L_1 for the lower-angle (leftmost) side are not

recorded. For rectangle 3, none of the vertical sides intercept the diffraction line. The case is a 'partial' diffraction because the intensities of L_1 for both the lower-angle (leftmost) and the higher-angle (rightmost) side are not recorded. The measured ranges in $\Delta\theta$ for 'semi-partial' and 'partial' situations are larger than R_θ.

To acquire a well defined useful multiple-beam profile on the two-beam intensity background (of the secondary reflection L) during the polar $\Delta\theta$ scan (see Fig. 4b), the angular range of scan, R_θ, has to be several times (about six times or more) the width of the primary reflection G (see Figs. 3a and 4a). The angle between the $\Delta\theta$ axis and the diffraction intensity line of the secondary reflection in the $(\Delta\theta, \Delta\psi)$ coordinate system is approximately equal to the angle α between the reciprocal-lattice vectors of G and L reflections (Cole et al., 1962). Therefore, to ensure a 'full' diffraction situation to occur, the angular range R_ψ has to be such that $R_\psi > R_\theta \tan\alpha$. All diffractions presented in Figs. 2, 4 and 5 are 'full' diffractions because they satisfy this condition.

For large $\tan\alpha$ and/or comparably small R_ψ, 'partial' diffraction usually occurs. Fig. 6(a) shows this situation for the systematic four-beam (000; 004; 13, 14, $\bar{5}$; 13, 14, 9) diffraction. The considerable decrease in the measured semi-integrated intensity is observed at both the tails of the profile. This profile
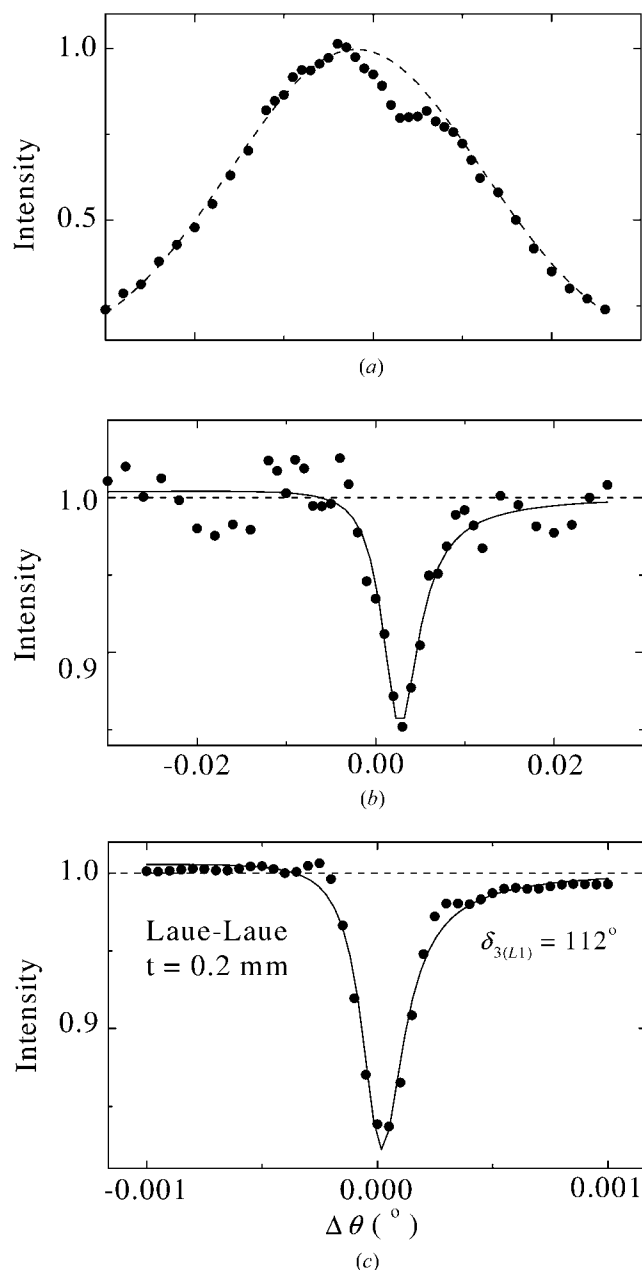

Figure 6
$\Delta\theta$ distribution of (a and b) measured and (c) calculated semi-integrated relative intensities for the L_1(13, 14, $\bar{5}$) reflection of four-beam (000; 004; 13, 14, $\bar{5}$; 13, 14, 9) case. (b) Intensity profile after subtracting a Gaussian (dashed curve of a) from the measured profile of (a). $|F_{13,14,5}| = 1127$, $|F_{13,14,9}| = 338$ and $|F_{0,0,14}| = 338$ and $|F_{0,0,14}| = 0$.
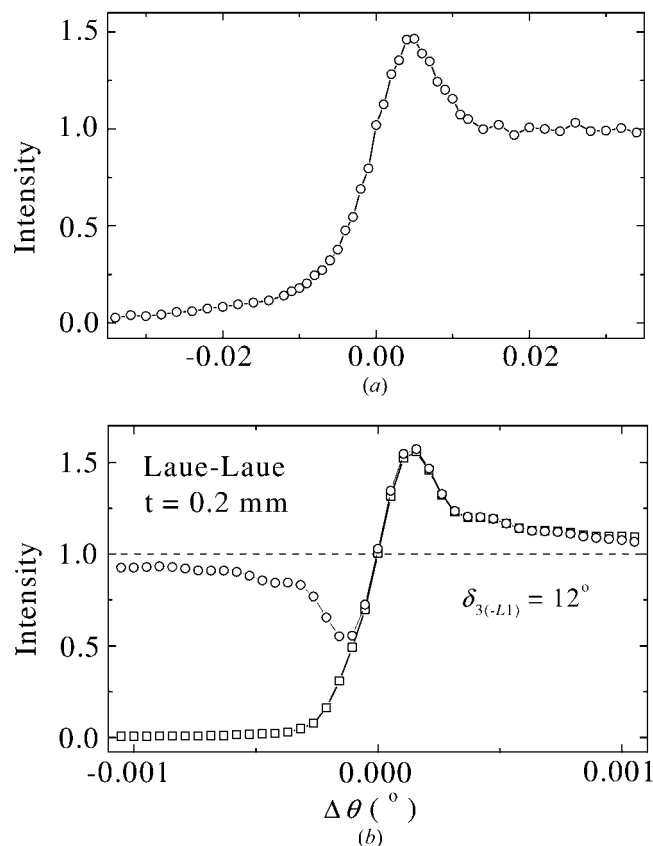

Figure 7
$\Delta\theta$ distribution of (a) measured and (b) calculated [open circles: 'full' profile; open squares: 'semi-partial' profile] semi-integrated relative intensities for the $L_1(8\bar{3}9)$ reflections of the four-beam (000; 00$\bar{4}$; $8\bar{3}9$; $\bar{8}35$) case. $|F_{839}| = 264$ and $|F_{835}| = 542$.

is quite different from those shown in Figs. 2, 4 and 5 for the 'full' diffraction situation. In the case when the profile tails do not coincide with the multibeam region (close to the central part of profile), the multibeam profile like a 'full' diffraction profile is still useful for phase estimation. By subtracting a Gaussian (the dashed curve of Fig. 6a) from the measured profile (solid circles of Fig. 6a), a new profile shown in Fig. 6(b) is obtained, exhibiting the phase-sensitive intensity variation due to multibeam interaction. For comparison, Fig. 6(c) shows the semi-integrated profile calculated for the 'full' diffraction situation. Unfortunately, this kind of subtraction is not universal. For different cases of 'partial' diffraction, the individual subtraction functions, like the combination of a Gaussian function with a constant background, needs to be used. Certainly, this fact reduces the practicality of using 'partial' diffraction for phase estimation.

Similar to the previous case in which $\tan \alpha$ is large and/or R_ψ is comparably small, a large shift of the multiple-beam position from the center of the $\Delta\psi$ scan range results. A 'semi-partial' diffraction can be encountered. Fig. 7 shows the measured and the calculated semi-integrated intensity distributions for the systematic four-beam $(000; 00\bar{4}; \bar{8}3\bar{9}; \bar{8}3\bar{5})$ diffraction. For a 'semi-partial' diffraction situation, these distributions (see Fig. 7a and the curve with open squares in Fig. 7b) show a profile with uneven tails, in contrast to the distribution of open circles calculated for a 'full' diffraction situation. This demonstrates clearly that the intensity decrease due to 'partial' diffraction strongly affects the multiple-beam region (the central part of profile). No phase information can be extracted from this kind of profile.

To sum up, with the aid of the dynamical calculation as a guide, 'partial' diffraction can be easily distinguished from 'full' diffraction. It is clear that for collecting a large number of multibeam diffraction data for phase estimation the azimuthal rotation and integration over a large angular range R_ψ is needed for realization of many 'full' diffraction situations.

6. Discussion and concluding remarks

The intensity variation of secondary reflections measured using stereoscopic multibeam imaging is, in general, weak compared to that obtained from primary reflections with the Renninger scan. The statistical error on the intensity measurement for the former is therefore relatively large. However, use of a better detector like CCD could improve the statistics and time-resolved intensity measurements could be carried out.

In conclusion, for collecting a large set of phase informative multibeam diffraction data for macromolecular crystals, the stereoscopic multibeam imaging technique for comparably strong primary reflections with intensity integration over the azimuthal angle is proposed. This integration suppresses the influence of neighboring multibeam diffractions on the measured intensity, and thus facilitates phase analysis. A simple practical method of quantitative estimation of the triplet reflection phases from multibeam profiles of ISR Friedel pairs is also proposed. With the help of dynamical calculation, the procedures for data handling and for distinguishing 'partial' diffraction images from 'full' diffraction images are developed considering the multibeam geometry and experimental conditions. These procedures can provide a practical way of reconstructing diffraction profiles for experimental phase estimation.

APPENDIX A

The laboratory coordinate system (x, y, z) is defined as follows. The incident beam is along the z axis and the upward vertical direction perpendicular to the incident beam is in the $+y$ direction. Facing the incident beam, the x axis, perpendicular to y and z axes, lies in the horizontal plane and is to the right. Suppose the three-beam (O, G, L) case occurs at $2\theta = 2\theta_G$, $\theta = \theta_G$, $\varphi = \varphi_O, \chi = \chi_O$. The position of the reciprocal-lattice point G is at $(-\cos\theta_G, 0, -\sin\theta_G)$ in the laboratory coordinate system. In order to find the angular position, 2θ, θ, $\varphi + \varphi_O$, χ, for the $(O, -G, -L)$ case, we could first move the crystal to the position at which the reciprocal-lattice vector $\mathbf{g}$ of the primary reflection G is along the $-x$ direction, represented as $[-1, 0, 0]$, and the secondary reciprocal-lattice vector $\mathbf{l} = [x, y, z]$ in the laboratory system. According to the inversion symmetry between the (O, G, L) and $(O, -G, -L)$, there are only two ways to find the position for the latter case to occur.

(i) Keeping the detector position unchanged, the reciprocal-lattice vectors $-\mathbf{g}$ and $-\mathbf{l}$ need to be moved to the original positions of $\mathbf{g} = [-1, 0, 0]$ and $\mathbf{l} = [x, y, z]$, or the equivalent positions for the (O, G, L) case. In other words, $\mathbf{g}$ and $\mathbf{l}$ need to be moved to $[1, 0, 0]$ and one of the equivalent positions $[\pm x, \pm y, \pm z]$, respectively. Considering the fact that two vectors $\mathbf{g}$ and $\mathbf{l}$ are changed simultaneously, only $[-x, y, -z]$, $[x, -y, -z]$ and $[-x, -y, z]$ with two 'minuses' are the possible positions for $\mathbf{l}$. Of these three, only $[-x, y, -z]$ is the correct equivalent vector position for $\mathbf{l}$ to move, because the position $[-x, -y, z]$ leads to no equivalent position for $-\mathbf{l}$ relative to $\mathbf{g}$. The position $[x, -y, -z]$ is the correct choice for $\mathbf{l}$ only when the detector position is changed from 2θ to -2θ [see item (ii)]. The rotation operations, leading to changing $\mathbf{g}$ to $[100]$ and $\mathbf{l}$ to $[-x, y, -z]$, are:

$$\mathbf{X}(\chi) \cdot (\varphi) \cdot \mathbf{X}(-\chi_0) \begin{pmatrix} -1 \\ 0 \\ 0 \end{pmatrix} = \begin{pmatrix} 1 \\ 0 \\ 0 \end{pmatrix} \qquad (7)$$

$$\mathbf{X}(\chi) \cdot (\varphi) \cdot \mathbf{X}(-\chi_0) \begin{pmatrix} x \\ y \\ z \end{pmatrix} = \begin{pmatrix} -x \\ y \\ -z \end{pmatrix}, \qquad (8)$$

where the χ circle is rotated $-\chi_O$ around the z axis back to its origin, the φ circle is rotated φ from φ_O around the $-x$ direction, and subsequently the χ circle is rotated χ from the origin around the z axis. The directions of rotation of the circles are referred to those defined for the 8-circle diffractometer used. Equation (7) gives

$$\begin{pmatrix} -\cos\chi_O\cos\chi - \cos\varphi\sin\chi_O\sin\chi \\ \cos\varphi\cos\chi\sin\chi_O - \cos\chi_O\sin\chi \\ -\sin\varphi\sin\chi_O \end{pmatrix} = \begin{pmatrix} 1 \\ 0 \\ 0 \end{pmatrix}. \quad (9)$$

This leads to

$$\varphi = 0, \quad \chi = \pm\pi + \chi_O \quad \text{or} \quad -\chi_O \quad (10a)$$

$$\varphi = \pi, \quad \chi = \pi - \chi_O \quad \text{or} \quad \chi_O. \quad (10b)$$

Only $\varphi = \pi$, $\chi = \pi - \chi_O$ in (10b) satisfies the condition imposed by (8). This means that the crystal needs to be rotated to $\varphi = \pi + \varphi_O$ and $\chi = -\chi_O$, while maintaining the same detector position as that for the (O, G, L) case.

(ii) Changing the detector position from 2θ to -2θ, **l** needs to be moved from $[x, y, z]$ to $[x, -y, -z]$ while **g** $= [-1, 0, 0]$ remains unchanged. The corresponding rotation operation are

$$\mathbf{X}(\chi)\cdot(\varphi)\cdot\mathbf{X}(-\chi_O)\begin{pmatrix} -1 \\ 0 \\ 0 \end{pmatrix} = \begin{pmatrix} -1 \\ 0 \\ 0 \end{pmatrix} \quad (11)$$

$$\mathbf{X}(\chi)\cdot(\varphi)\cdot\mathbf{X}(-\chi_O)\begin{pmatrix} x \\ y \\ z \end{pmatrix} = \begin{pmatrix} x \\ -y \\ -z \end{pmatrix}. \quad (12)$$

Equation (12) gives

$$\begin{pmatrix} -\cos\chi_O\cos\chi - \cos\varphi\sin\chi_O\sin\chi \\ \cos\varphi\cos\chi\sin\chi_O - \cos\chi_O\sin\chi \\ -\sin\varphi\sin\chi_O \end{pmatrix} = \begin{pmatrix} -1 \\ 0 \\ 0 \end{pmatrix}. \quad (13)$$

This leads to

$$\varphi = 0, \quad \chi = \chi_O \quad \text{or} \quad \pi - \chi_O \quad (14a)$$

$$\varphi = \pi, \quad \chi = -\chi_O \quad \text{or} \quad \pm\pi + \chi_O. \quad (14b)$$

Only $\varphi = \pi$, $\chi = \chi_O$ in (14b) satisfies the condition of (12). This implies that the crystal needs to be rotated to $\varphi = \pi + \varphi_O$, and $\chi = -\chi_O$, while moving the detector from 2θ to -2θ.

References

Bricogne, G. & Gilmore, C. J. (1990). *Acta Cryst.* A**46**, 284–297.
Chang, S. L. (1984). *Multiple Diffraction of X-rays in Crystals.* Berlin: Springer-Verlag.
Chang, S. L. (1987). *Crystallogr. Rev.* **1**(2), 85–190.
Chang, S. L. (1998). *Acta Cryst.* A**54**, 886–894.
Chang, S. L., Chao, C. H., Huang, Y. S., Jean, Y. C., Sheu, H. S., Liang, F. J., Chien, H. C., Chen, C. K. & Yuan, H. S. (1999). *Acta Cryst.* A**55**, 933–938.
Chang, S. L., Huang, Y. S., Chao, C. H., Tang, M. T. & Stetsko, Yu. P. (1998). *Phys. Rev. Lett.*, **80**, 301–304.
Chang, S. L., King, H. E., Huang, M. T. & Gao, Y. (1991). *Phys. Rev. Lett.* **67**, 3113–3116.
Chang, S. L., Stetsko, Yu. P., Huang, Y. S., Chao, C. H., Liang, F. J. & Chen, C. K. (1999). *Phys. Lett. A*, **264**, 328–333.
Chang, S. L. & Tang, M. T. (1988). *Acta Cryst.* A**44**, 1065–1072.
Chang, S. L. & Wang, C. M. (1996). *Acta Cryst.* A**52**, C52.
Cole, H., Chambers, F. W. & Dunn, H. M. (1962). *Acta Cryst.* **15**, 138–144.
Colella, R. (1992) *P. P. Ewald and his Dynamical Theory of X-ray Diffraction*, edited by D. W. J. Cruickshank, H. J. Juretschke & N. Kato, pp. 71–78. IUCr/Oxford University Press.
Han, F. S. & Chang, S. L. (1983). *Acta Cryst.* A**39**, 98–101.
Hölzer, K., Weckert, E. & Schroer, K. (2000). *Acta Cryst.* D**56**, 322–327.
Hümmer, K., Bondza, H. & Weckert, E. (1991). *Z. Kristallogr.* **195**, 169–188.
Kossel, W. (1936). *Ann. Phys. (Leipzig)*, **26**, 533–553.
Kov'ev, E. K., Andreev, A. V. & Deigen, M. I. (1984). *Sov. Phys. Solid State*, **26**, 1927–1928.
Larsen, H. B. & Thorkildsen, G. (1998a). *Acta Cryst.* A**54**, 129–136.
Larsen, H. B. & Thorkildsen, G. (1998b). *Acta Cryst.* A**54**, 137–145.
Mo, F., Mathiesen, R. H., Alzari, P. M., Lescar, J. & Rasmussen, B. (1998). *Materials Structure in Chemistry, Biology, Physics and Technology*, Vol. 5, edited by R. Kuzel, J. Lhotha & L. Dobiasova, p. 484. Praha: Czech and Slovak Crystallographic Association.
Renninger, M. (1937). *Z. Kristallogr.* **97**, 107–121.
Schenk, H. (1991). Editor. *Direct Methods for Solving Crystal Structures.* New York: Plenum Press.
Shen, Q. (1998). *Phys. Rev. Lett.* **80**, 3268–3271.
Shen, Q., Kycia, S. & Dobrianov, I. (2000). *Acta Cryst.* A**56**, 264–267.
Stetsko, Y. P. & Chang, S. L. (1997). *Acta Cryst.* A**53**, 28–34.
Thorkildsen, G. & Larsen, H. B. (1998). *Acta Cryst.* A**54**, 120–128.
Thorkildsen, G. Larsen, H. B. & Weckert, E. (2001). *Acta Cryst.* A**57**, 389–394.
Wang, C. M, Chao, C. H. & Chang, S. L. (2001). *Acta Cryst.* A**57**, 420–428.
Weckert, E., Hölzer, K., Schroer, K., Zellner, J. & Hümmer, K. (1999). *Acta Cryst.* D**55**, 1320–1328.
Weckert, E. & Hümmer, K. (1997). *Acta Cryst.* A**53**, 108–143.
Weeks, C. M., Xu, H., Hauptman, H. A. & Shen, Q. (2000). A**56**, 280–283.